Tumor establishment requires tumor autonomous and non-autonomous decoupling of EGF signaling from apoptosis

Sang Ngo[1]*, Jackson Liang[1]*, & Lucy Erin O'Brien[1]†

[1] Department of Molecular and Cellular Physiology, Stanford University School of Medicine, Stanford, California 94305, USA.

* These authors contributed equally to this work
† Corresponding author (lead contact)

Summary

During organ turnover, robust mechanisms enforce a balanced equilibrium between cell division and death [1, 2]. Nascent tumors must destabilize these mechanisms to subvert cell equilibrium for cancerous growth [3-7]. The nature of these destabilizing events is central to understanding how new tumors become established and may suggest strategies for cancer prevention. One of the best characterized mechanisms for cell equilibrium is that of the adult *Drosophila* intestine. In this organ, division is coupled to death because Rhomboid, a protease that cleaves mitogenic EGFs for secretion, is induced in cells undergoing apoptotic elimination [8]. In *Drosophila*, as in mammals, intestinal stem cells give rise to adenomas following loss of adenomatous polyposis coli (APC) [9]. Examining *Drosophila APC*$^{-/-}$ tumorigenesis, we find that pre-tumor cells destabilize cell equilibrium by uncoupling *rhomboid* from apoptosis, which creates feed-forward amplification of EGF signaling for tumor establishment. Prior to tumor formation, *APC*$^{-/-}$ cells induce *rhomboid* in surrounding cells via activation of the stress signal JNK. During subsequent growth, *APC*$^{-/-}$ tumors induce *rhomboid* within the tumor itself via loss of E-cadherin and consequent activity of p120-catenin. Chronic induction of *rhomboid* in both tumor and surrounding cells leads to constitutive activation of EGFR and is essential for tumors to progress. Thus, incipient tumors combine non-autonomous and autonomous strategies to deregulate *rhomboid* and destabilize cell equilibrium. Since Rhomboid, EGFR, and E-cadherin are associated with colorectal cancer in humans [10-17], our findings may shed light on how human colorectal tumors progress.

Results and Discussion

To investigate how tumors subvert cell equilibrium in the *Drosophila* intestine (midgut), we generated intestinal stem cells that were null for *APC* (Figures 1A, S2A) and allowed them to initiate tumorigenesis. Low-frequency, *hs-flp*-mediated MARCM recombination [18] was used to produce a sparse distribution of stem cells that were (1) marked by heritable expression of GFP and (2) either control genotype or else homozygous for null alleles of *Drosophila APC1* and *APC2* (*APC*$^{-/-}$) [19, 20] (Figure S2A).

As described previously [21-25], *APC*$^{-/-}$ stem cells frequently gave rise to multilayered adenomas over a period of 2-3 weeks (Figure S1B-E). At 2 days after induction, all *APC*$^{-/-}$ clones were single-layered (Figure S1E). By 5 days after induction, 6.8 $\pm$ 1.9% of *APC*$^{-/-}$ clones were multilayered. By 21 days after induction, 36.2 $\pm$ 1.7% of *APC*$^{-/-}$ clones were multilayered. In addition, *APC*$^{-/-}$ clones grew larger than control clones. Whereas most 21-day control clones contained fewer than 50 cells, many 21-day *APC*$^{-/-}$ clones contained 100-500 cells (Figure 1G). These large, multilayered clones formed prominent masses that protruded into the midgut lumen (Figure S1D), a phenotype reminiscent of *APC*-inactivated colonic adenomas in humans [26].

As human *APC* cancers progress, they often lose expression of the tumor suppressor E-cadherin [27, 28]. We therefore examined whether *APC*$^{-/-}$ tumors in the *Drosophila* midgut exhibit loss of *E-cad* (also known as *shotgun*). In control tissue, E-cad::mTomato [29] localized prominently to lateral cell membranes, as expected (Figure 1B) [8]. In *APC*$^{-/-}$ clones that were single-layered, E-cad::mTomato also localized to lateral membranes, consistent with prior work [22] (Figure 1C). In *APC*$^{-/-}$ clones that were multilayered, however, E-cad::mTomato localized to membranes inconsistently and, in supra-basal layers, was often absent (Figures 1B, 1C). These observations suggest that *Drosophila APC*$^{-/-}$ tumors, like their human counterparts, downregulate E-cad as they become more advanced.

Since human E-cad is an epithelial tumor suppressor, we wondered whether forced expression of *E-cad* would suppress tumor formation. To test this possibility, we

generated *APC*$^{-/-}$ stem cells that additionally overexpressed *E-cad* and assessed their tumorgenicity (Figures 1D, S3A). *APC*$^{-/-}$, *E-cad* stem cells gave rise to clones that were markedly smaller than those generated by *APC*$^{-/-}$ stem cells (Figures 1F, 1G). Furthermore, *APC*$^{-/-}$, *E-cad* clones generally maintained normal tissue structure. Whereas many *APC*$^{-/-}$ clones became multilayered after 21 days, the vast majority of *APC*$^{-/-}$, *E-cad* clones remained single-layered (Figure 1H). Thus, analogous to human epithelia, *E-cad* acts as a tumor suppressor in the *Drosophila* midgut.

We sought to determine how *E-cad* suppresses midgut tumorigenesis. A prevailing model is that loss of E-cad promotes tumor progression by weakening cell-cell adhesion to enable tumor cell invasion. To test whether tumor suppression by E-cad involves adhesion, we forced *APC*$^{-/-}$ stem cells to overexpress *E-cad*^{dCR4h}, an allele that lacks extracellular adhesion motifs (Figure 1E) [30]. Despite being adhesion-incompetent, *E-cad*^{dCR4h} was equally as effective as wild-type *E-cad* at preventing *APC*$^{-/-}$ clone overgrowth and multilayering (Figures 1G, 1H). These results show that tumor suppression by *Drosophila* E-cad does not require cadherin-mediated extracellular adhesion.

We considered an alternate model in which E-cad suppresses tumorigenesis by binding p120-catenin (p120) [31]. During steady-state turnover, E-cad inhibits the transcriptional activity of p120 [8] (Figure S1A), likely by sequestering it at the cortex of mature enterocytes. This interaction prevents p120 from inducing *rhomboid*, an intracellular protease whose expression enables secretion of EGFs and consequent divisions of stem cells [8].

To test the role of the E-cad-p120 interaction in tumor suppression, we forced *APC*$^{-/-}$ stem cells to express *E-cad*$^{\Delta JM}$, an allele with a juxtamembrane deletion that abrogates binding of p120 but not α-catenin or β-catenin (also known as Armadillo) [32]. Unlike *E-cad* and *Ecad*^{dCR4h}, *E-cad*$^{\Delta JM}$ failed to suppress tumorigenesis. *APC*$^{-/-}$, *E-cad*$^{\Delta JM}$ clones grew to sizes comparable to *APC*$^{-/-}$ clones, and a similar proportion became multilayered (Figures 1G, 1H). These findings imply that binding of E-cad to p120 is crucial for tumor suppression.

Another E-cadherin-associated transcription factor, β-catenin, is known to contribute to *APC*-driven tumorigenesis in both *Drosophila* midgut and mammalian intestine [21, 22, 33, 34] However, β-catenin indiscriminately associates with E-cad alleles that are tumor-suppressive (*E-cad* and $Ecad^{dCR4h}$) and with alleles that are tumor non-suppressive ($E\text{-}cad^{\Delta JM}$) (Figure 1E). Thus, the capacity for each *E-cad* to rescue tumor growth cannot be attributed to differences in β-catenin sequestration.

If the E-cad-p120 interaction suppresses tumorigenesis by sequestering p120, then loss of *p120* should also suppress tumorigenesis. To test this prediction, we depleted *p120* from $APC^{-/-}$ stem cells using RNAi. Double $APC^{-/-}$, *p120RNAi* clones accumulated significantly fewer cells and exhibited less multilayering compared to $APC^{-/-}$ clones (Figures 1G, 1H). These findings, combined with the loss of tumor suppression by $E\text{-}cad^{\Delta JM}$, imply that downregulation of E-cad promotes tumorigenesis by deregulating p120.

We had previously identified that p120 activates transcription of *rhomboid* in apoptotic enterocytes during steady-state turnover [8]. Since p120 is necessary for $APC^{-/-}$ tumor development, we wondered whether *rhomboid* is also necessary. First, we examined expression of a *rhomboid-lacZ* reporter (Figure 2A). Flp/FRT recombination was used to generate unlabeled, $APC^{-/-}$ stem cells in a background of GFP-labeled cells (Figure S2B) [24]; both $APC^{-/-}$ and background cells possessed the *rhomboid-lacZ* transgene.

We observed widespread expression of *rhomboid* in midguts containing $APC^{-/-}$ tumors. After 21 days of clone development, *rhomboid* was expressed by 15.3 ± 12.4% of cells in $APC^{-/-}$ clones but only 1.7 ± 3.4% of cells in control clones (Figures 2A-C). Furthermore, in midguts that contained $APC^{-/-}$ clones, *rhomboid* was expressed by 20.0 ± 12.7% of non-clone background cells, whereas in midguts that contained control clones, *rhomboid* was expressed by only 2.1 ± 1.7% of background cells (Figures 2B, 3A). Thus as $APC^{-/-}$ tumors develop, *rhomboid* becomes hyper-induced both tumor autonomously and non-autonomously.

Our prior work showed that during normal turnover, *rhomboid* is suppressed in healthy enterocytes and induced in apoptotic enterocytes (Figure S1A) [8]. This regulatory mechanism gives rise to tissue-level cell equilibrium by spatiotemporally coupling the release of EGFs that are essential for stem cell division to the loss of terminally differentiated cells that need replacement. Since cell equilibrium must be disrupted for tumors to form, we wondered whether regulated expression of *rhomboid* was also disrupted.

Examining midguts with *APC*$^{-/-}$ clones, we observed that the vast majority of *rhomboid*-expressing cells were non-apoptotic. In *APC*$^{-/-}$ clones, 92.7 $\pm$ 3.7% of *rhomboid*-expressing cells lacked caspase activation (Figure 2D). In the tissue surrounding *APC*$^{-/-}$ clones, 89.0 $\pm$ 2.9% of *rhomboid*-expressing background cells lacked caspase activation (Figure 3B). These findings imply that tumor-associated hyper-induction of *rhomboid*, unlike steady-state induction of *rhomboid*, does not require apoptosis.

Since Rhomboid enables EGF secretion, hyper-induction of *rhomboid* should lead to hyperactivation of EGFR. To test this prediction, we performed immunostaining for the activated, di-phosphorylated form of the EGFR effector Erk (dpErk) [4, 8, 22, 35]. We found that 30.7 $\pm$ 17.0% of cells in *APC*$^{-/-}$ clones exhibited dpErk, compared to just 5.5 $\pm$ 7.1% of cells in control clones (Figures 2E, 2F). Background cells also exhibited dpErk more frequently in midguts with *APC*$^{-/-}$ clones compared to midguts with control clones (Figures 2E). Thus, hyperactivation of EGFR accompanies hyper-induction of *rhomboid* during *APC*$^{-/-}$ tumorigenesis.

Does hyper-induction of *rhomboid* drive *APC*$^{-/-}$ tumorigenesis? We first examined whether developing tumors require tumor-autonomous *rhomboid* production. MARCM was used to generate GFP-labeled, *APC*$^{-/-}$ stem cells that were additionally depleted of *rhomboid* (Figure S3A). These *APC*$^{-/-}$, *rhomboid*-knockdown stem cells formed clones that were smaller than those formed by *APC*$^{-/-}$ stem cells (Figures 2G, 2H). Moreover, the vast majority of *APC*$^{-/-}$, *rhomboid*-knockdown clones did not become multilayered (Figure 2I). Consistent with these phenotypes, depletion of *egfr* from *APC*$^{-/-}$ stem cells also prevented clone growth and multilayering (Figures 2G, 2H, 2I), similar to prior

reports [4, 22, 35]. Thus, hyper-induction of *rhomboid* within nascent *APC*$^{-/-}$ tumors is required for tumor growth and progression, likely via hyperactivation of EGFR.

We next assessed whether tumor development requires non-autonomous production of *rhomboid* in background cells. To manipulate gene expression specifically in background cells and not in *APC*$^{-/-}$ tumor cells, RU486-inducible RNAi knockdown in background cells was combined with Flp/FRT recombination to generate *APC*$^{-/-}$ stem cells that were unresponsive to RU486 (Figures 3C, S2C, S3B) [24]. Additional inclusion of a recombination-sensitive RFP transgene enabled background cells and *APC*$^{-/-}$ cells to be distinguished as RFP-labeled and unlabeled, respectively.

Using this system, we found that depletion of *rhomboid* in background cells caused a marked reduction in both the sizes of *APC*$^{-/-}$ clones and the frequency of *APC*$^{-/-}$ clones that became multilayered (Figures 3D, 3E, 3F). Depletion of *p120* or overexpression of *E-cad* had similar effects (Figures 3D, 3E, 3F), consistent with observed loss of *E-cad::mTomato* in patches of background cells. Depletion of *egfr*, on the other hand, did not alter either the sizes of *APC*$^{-/-}$ clones or the frequency of multilayering (Figures 3D, 3E, 3F). Thus Rhomboid, but not Egfr, is required in background cells for tumors to progress.

These findings provide insight into how cell equilibrium becomes destabilized for tumor formation. The requirement for *egfr* in tumor cells and not background cells implies that tumor growth is driven by tumor-autonomous hyperactivation of EGFR. By contrast, the dual requirement for *rhomboid* in tumor cells and in background cells suggests that non-apoptotic cells in both populations must chronically produce EGFs to overcome robust mechanisms of cell equilibrium.

How do incipient tumors incite non-apoptotic background cells to express *rhomboid*? An appealing possibility involves stress signaling via the Jun N-terminal kinase (JNK; also *basket* or *bsk* in *Drosophila*). Prior work has shown that growth of *APC*$^{-/-}$ tumors requires JNK in both tumor cells and background cells [24]. Furthermore, regeneration of damaged midguts is accompanied by widespread induction of *rhomboid* [36, 37]. These precedents raise the possibility that *APC*$^{-/-}$ cells influence background cells to express *rhomboid* via JNK.

To investigate this possibility, we compared the kinetics of JNK and *rhomboid* in background cells as tumors developed over time. Unmarked *APC*$^{-/-}$ stem cells were generated in a background of GFP-labeled cells using Flp/FRT recombination (Figure S2B). Midguts were harvested at 2, 5, 10, or 21 days after clone induction (Figure 4A), and background cells were immunostained for activated, phosphorylated JNK (pJNK) and *rhomboid-lacZ* (Figures 4B, 4C, 4D).

After 2 days of clone growth, few background cells exhibited either pJNK or *rhomboid-lacZ*. At 5 days, the number of pJNK^{+} background cells had climbed sharply while the number of *rhomboid-lacZ*$^{+}$ background cells was still low. Between 5-21 days, pJNK^{+} background cells remained high, while *rhomboid-lacZ*$^{+}$ background cells had increased markedly. Thus, background cells activate JNK before they hyper-induce *rhomboid*.

Interestingly, both JNK activation and *rhomboid* hyper-induction occurred in background cells before occurring in *APC*$^{-/-}$ cells (Figure 4B). Furthermore, at 5 days after clone induction, when activated JNK was first detected in background cells (Figures 4B, 4C), the morphology of *APC*$^{-/-}$ clones still resembled control clones. This timing suggests that nascent *APC*$^{-/-}$ clones elicit non-autonomous JNK activation in their neighbors even before the clones form multilayered tumors.

We noticed that, 5-21 days after clone induction, pJNK was exhibited by ~80% of *rhomboid*-expressing background cells (Figure 4E). This high coincidence raised the possibility that JNK acts directly in background cells to induce *rhomboid*. To test this notion, the genetic system in Figures S2C and S3B was used to generate *APC*$^{-/-}$ stem cell clones and, concomitantly, inhibit JNK in background cells via expression of dominant negative *bsk* (*bsk*^{DN}) [38, 39]. Expression of *bsk*^{DN} specifically in background cells was sufficient to decrease levels of *rhomboid* mRNA by ~40% (Figure 4F). Since *rhomboid* is essential for tumorigenesis, we conclude that incipient tumors enable their own growth by JNK-mediated induction of *rhomboid* in surrounding cells.

Perspective

In summary, we have shown that *APC*$^{-/-}$ cells require both autonomous and non-autonomous deregulation of the EGF protease *rhomboid* to disrupt cell equilibrium and generate tumors. Before *APC*$^{-/-}$ cells develop into tumors, they induce *rhomboid* in non-apoptotic background cells by activating JNK. Once tumors are established, they autonomously activate *rhomboid* via loss of E-cadherin and release of p120-catenin. Deregulation of *rhomboid* in both tumor cells and background cells is required for multilayered adenomas to form. This dual requirement implies that high levels of EGFs are necessary to subvert robust mechanisms of cell equilibrium.

During steady-state turnover, precisely regulated induction of *rhomboid* controls cell equilibrium by coupling division to death: Because *rhomboid* is normally induced in cells undergoing apoptotic elimination, mitogenic EGFs are produced at the specific time and place that replacement cells are needed. For *APC*$^{-/-}$ cells to disrupt cell equilibrium, they must instigate widespread induction of *rhomboid* in cells that are non-apoptotic (Figure 4G). Non-apoptotic induction of *rhomboid* effectively decouples cell division from cell death by enabling EGFs to be produced chronically. Constitutive production of EGFs drives continual production of new cells irrespective of tissue need.

This mechanism of *APC*$^{-/-}$ tumor establishment in *Drosophila* may shed light on initiation of human colorectal cancers, which are tightly associated with inactivating mutations in *APC*. Intriguingly, Rhomboids, E-cadherin, and EGFR have all been implicated in progression of the human disease [13, 17, 40-42], suggesting that this tumorigenic signaling axis may be conserved. In this regard, two of our findings carry particular interest: First, while loss of E-cad is canonically thought to promote metastasis via loss of cell-cell adhesion, our findings reveal a new role during early-tumor development: deregulation of p120-catenin to drive EGF signaling. To our knowledge, the role of p120-catenin in colorectal cancer has not been investigated. Second, we find that induction of *rhomboid* is a tumor-initiating event, whereas studies of mammalian Rhomboids have focused on advanced cancers. Examining Rhomboids in early-stage mammalian tumorigenesis could be fruitful. Overall, understanding how

incipient tumors destabilize cell equilibrium may suggest new strategies for preventing cells with tumor-initiating potential from becoming established tumors.

Additional Information

Acknowledgements

S.N. was supported by Stanford Bio-X Undergraduate Fellowship. J.L. was supported by NSF GRFP DGE-114747 and NIH T32GM007276. This work was supported by ACS RSG-17-167-01-DDC, NIH R01GM116000-01A1, and a Stanford VPUE Faculty Grant to L.E.O. Confocal microscopy was performed at the Stanford Beckman Cell Sciences Imaging Facility (NIH 1S10OD01058001A1). We thank D. Bilder for the gift of cCas-3 antibody; the Developmental Studies Hybridoma Bank for other antibodies; M. Peifer, E. Piddini, M. Fuller, H. Jiang, the Bloomington *Drosophila* Stock Center (NIH P40OD018537), the TRiP at Harvard Medical School (NIH/NIGMS R01-GM084947), and the Vienna *Drosophila* Resource Center (http://stockcenter.vdrc.at/control/main) for fly stocks; M. Mirvis, L.J. Koyama, and E.N. Sanders for helpful discussions; and J. Cordero and K. Campbell for comments on the manuscript. The authors declare no competing interests.

Author Contributions

J.L., S.N., and L.E.O. designed the study. J.L. and L.E.O. wrote the manuscript. S.N. performed genetic crosses, tissue dissection and immunostaining. J.L. designed the experiments, built fly lines, performed qPCR experiments, quantitative analysis of microscopy data, and statistical analysis. S.N. and J.L. performed confocal microscopy on tissues.

Author Information

The authors declare no competing financial interests. Correspondence and requests for materials should be addressed to L.E.O. (lucye@stanford.edu).

Figures 1-6

Figure 1

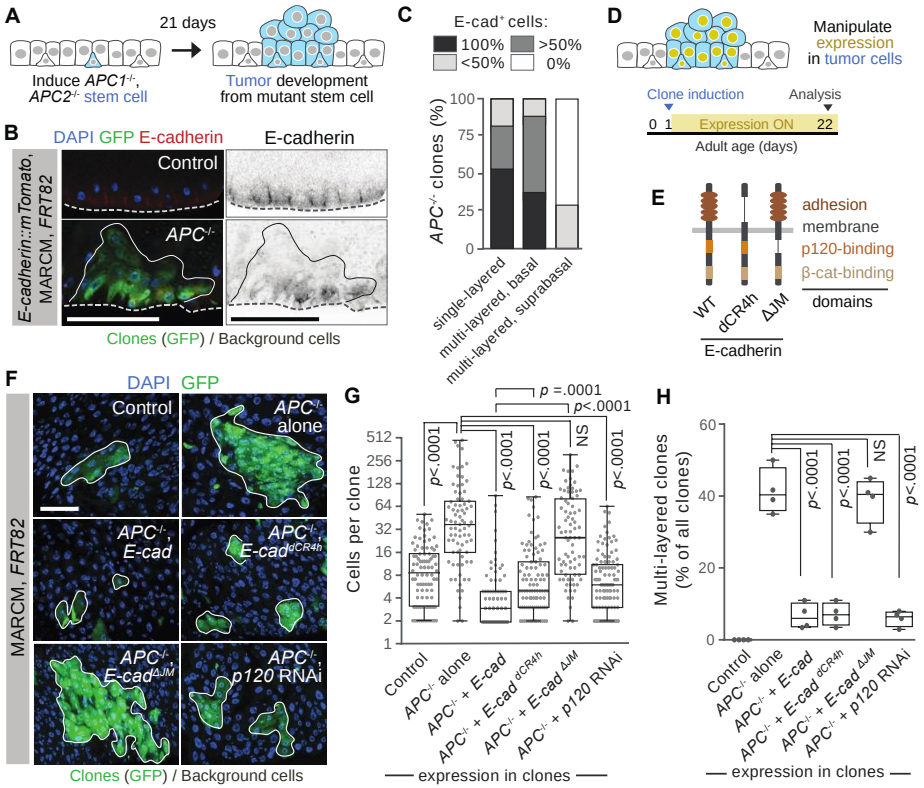

Figure 1. Growth of multilayered *APC*$^{-/-}$ tumors requires tumor-autonomous downregulation of E-cadherin and consequent deregulation of p120-catenin.

(A) Experimental schema for B and C. Sparsely distributed, GFP-marked stem cells are null for both *APC1* and *APC2* (*APC*$^{-/-}$). Over the next 21 days, many of these stem cells develop into GFP-marked, multilayered adenomas. See Figures S1, S2A for genetic strategy.

(B) Loss of E-cadherin in supra-basal layers of *APC*$^{-/-}$ tumors. E-cad::mTomato (red) is expressed in control tissue (top panels) and in basally localized cells within multilayered *APC*$^{-/-}$ clones (bottom panels; GFP, green) but is absent from supra-basal cells. Dotted line indicates the basement membrane.

(C) Frequency of E-cad::mTomato expression within *APC*$^{-/-}$ clones. Percentages of all *APC*$^{-/-}$ cells that exhibit E-cad::mTomato are shown for single-layered clones, basal layers of multilayered clones, and supra-basal layers of multilayered clones. 67 single-layered tumors and 38 multilayered *APC*$^{-/-}$ clones pooled from *n* = 4 midguts at 21 days post-induction.

(D) Experimental schema for F-H. GFP-marked, *APC*$^{-/-}$ stem cells are generated at 1 day post-eclosion, and gene expression is manipulated specifically within these cells. At 22 days post-eclosion (21 days post-induction), the resulting, GFP-marked stem cell clones are analyzed. See Figures S2A and S3A for genetic strategy.

(E) Domain structure of wild-type (wt) E-cad and mutant E-cad alleles that lack either the extracellular adhesion domain (*E-cad*^{dCR4h}) [30] or the intracellular binding domain for p120-catenin (*E-cad*$^{\Delta JM}$) [32].

(F-H) Forced expression of *E-cad* in *APC*$^{-/-}$ clones inhibits tumor growth and multilayering in a p120-dependent, adhesion-independent manner. Images **(F)** and quantification **(G)** of sizes of clones with the indicated genotypes. Cells in clones are marked by GFP. Clone boundaries are outlined in white. In G, *n* = 3 midguts per genotype; *P* values by Mann-Whitney *U*-test. **(H)** Frequency of multilayered clones as a percentage of total clones. *n* = 4 midguts per genotype. *P* values by unpaired *t*-test.

For **(C**, **G**, **H)**, one of three independent experiments is shown with n midguts per experiment as indicated. For box-and-whisker plots, boxes show median, 25th and 75th percentiles, and whiskers are minimum and maximum values. Representative images shown in each panel. All scale bars, 50 µm.

Figure 2

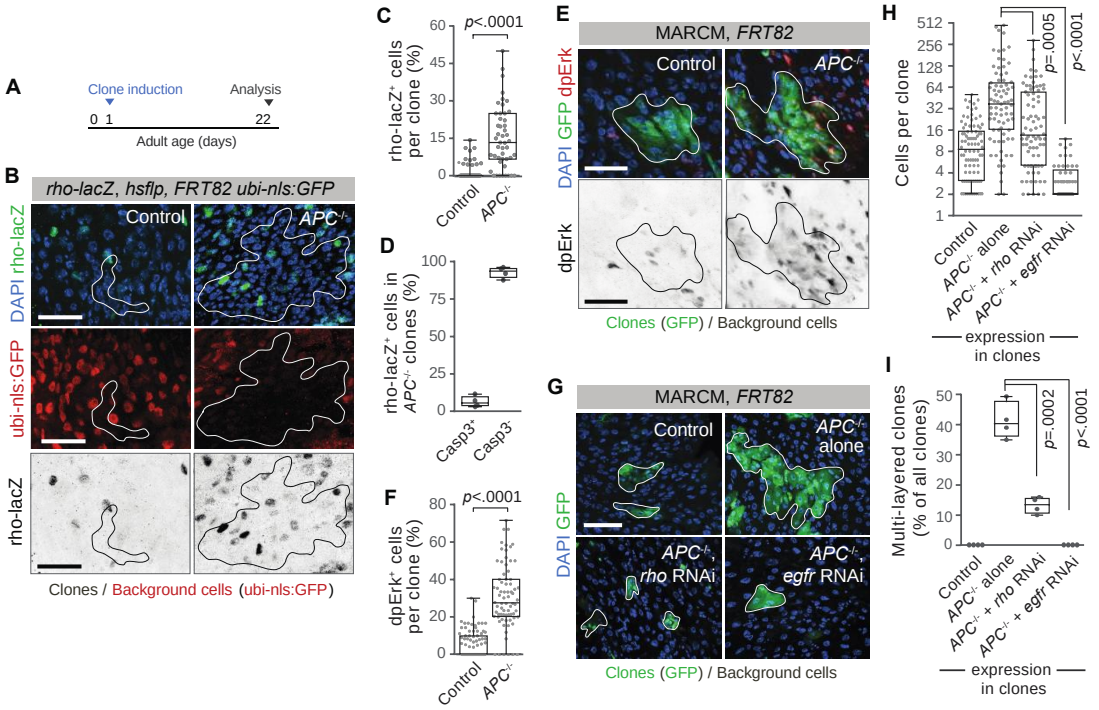

Figure 2. Hyperactivation of *rhomboid* and Egfr in non-apoptotic *APC*$^{-/-}$ cells is essential for tumor growth and multilayering.

(A) Experimental timeline for B-I. Clones are induced at 1 day post-eclosion and midguts are analyzed at 22 days post-eclosion (21 days post-induction).

(B-C) Cells in *APC*$^{-/-}$ clones express *rhomboid* more frequently than cells in control clones. **(B)** Immunostaining for a *rhomboid-lacZ* reporter (*rho-lacZ*; green in top row, inverted grayscale in bottom row) in midguts with control clones (left column) and *APC*$^{-/-}$ clones (right column). Clone boundaries are outlined in white (top and middle rows) and black (bottom row). Cells in clones lack GFP; background, non-clone cells are marked by GFP (red pseudocolor). See Figure S2B for genetic strategy. **(C)** Percentage of cells per clone that express *rhomboid-lacZ*. In the control dataset, 42 clones contain zero cells that express *rhomboid-lacZ* (0%). Clones from n = 3 midguts per genotype; P values by Mann-Whitney U-test.

(D) Most *rhomboid*-expressing *APC*$^{-/-}$ cells are non-apoptotic, as revealed by immunostaining against cleaved Caspase3 (Casp3). Graph shows the percentages of all *rhomboid-lacZ*$^{+}$, *APC*$^{-/-}$ cells per midgut that are apoptotic (Casp3^{+}) and non-apoptotic (Casp3$^{–}$). *n* = 4 midguts.

(E-F) Cells in *APC*$^{-/-}$ clones activate Erk more frequently than cells in control clones. **(E)** Erk activation was assessed by immunostaining for diphosphorylated Erk (dpErk) (top row, red; bottom row, inverted grayscale). Cells in clones are marked by GFP (green, top row). Clone boundaries are outlined in white (top row) and black (bottom row). See Figure S2A for genetic strategy. **(F)** Percentages of cells per clone that exhibit dpErk. In the control dataset, 47 clones contain zero dpErk^{+} cells (0%). Clones from *n* = 3 midguts per genotype; *P* values by Mann-Whitney *U*-test.

(G-I) Tumor growth and multilayering requires tumor-autonomous *rhomboid* and *egfr*. Images **(G)** and sizes **(H)** of clones with the indicated genotypes. Cells in clones are marked by GFP (green). Clone boundaries are outlined in white. *rhomboid* and *egfr* RNAi, where indicated, was performed specifically within clone cells. See Figures S2A and S3A for genetic strategy. In **(H)**, *n* = 3 midguts per genotype; *P* values by Mann-Whitney *U*-test. **(I)** Frequency of multilayered clones as a percentage of total clones. *n* = 4 midguts per genotype. *P* values by unpaired *t*-test.

For **(C-D, F, H-I)**, one of three independent experiments is shown with *n* samples as specified for each experiment. For box-and-whisker plots, the boxes show median, 25th and 75th percentiles, and whiskers are minimum and maximum values. Representative images shown in each panel. All scale bars, 50 µm.

Figure 3

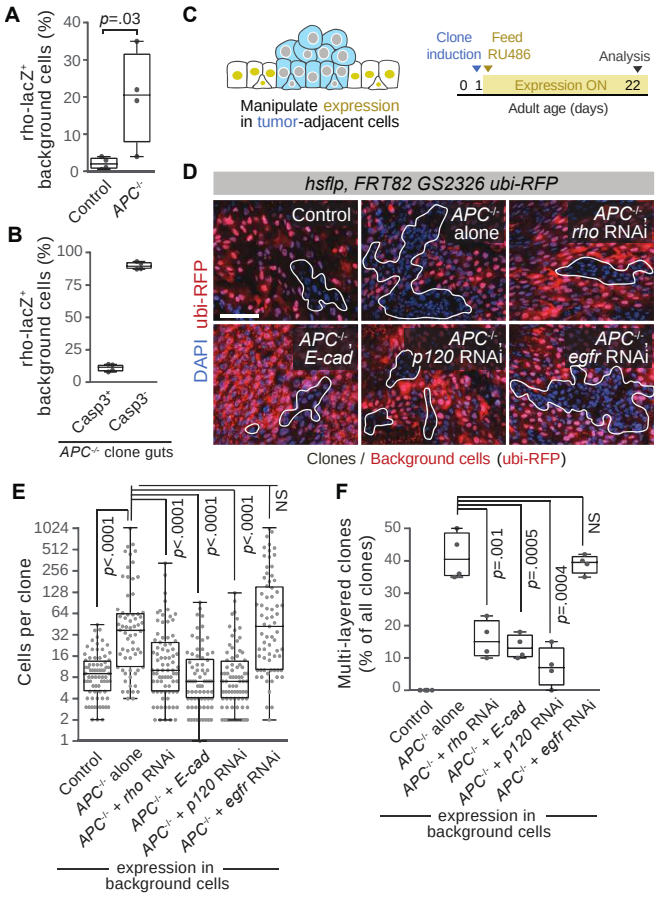

Figure 3. Hyperactivation of *rhomboid* but not Egfr in non-apoptotic background cells is essential for tumor growth and multilayering.

(A) Background cells express *rhomboid* more frequently in midguts with *APC*$^{-/-}$ clones than in midguts with control clones. Control and *APC*$^{-/-}$ midgut clones were induced using the same experimental protocol and genotypes as Figures 2A-C. Each data point shows the percentage of all background cells that are *rhomboid-lacZ*$^{+}$ in one midgut. Data points in Figures 3A and 2C were obtained from the same midguts. n = 4 midguts per genotype. P values by unpaired t-test.

(B) In midguts with *APC*$^{-/-}$ clones, most *rhomboid*-expressing background cells are non-apoptotic. Graph shows percentages of all *rhomboid-lacZ*$^{+}$ background cells per midgut that are apoptotic (Casp3^{+}) and non-apoptotic (Casp3$^{–}$), as assessed by immunostaining. *n* = 4 midguts per genotype. *P* values by unpaired *t*-test.

(C-F) Tumor growth and multilayering requires tumor non-autonomous *rhomboid* but not *egfr*. **(C)** Timeline for concomitant generation of *APC*$^{-/-}$ clones and genetic manipulation of background cells. *APC*$^{-/-}$ stem cells are induced at 1 day post-eclosion. Immediately after induction, RU486 is administered to activate exogenous gene expression in background cells. RU486 administration continues until midguts are analyzed 22 days post-eclosion (21 days post-induction). See Figures S2C, S3B for genetic strategy. **(D-E)** Images **(D)** and sizes **(E)** of clones with the indicated genotypes. Cells in clones lack RFP; background cells are marked by RFP (red). Clone boundaries are outlined in white. RNAi, where indicated, was performed specifically within background cells. Scale bar, 50 µm. In **(E)**, *n* = 3 midguts per genotype; *P* values by Mann-Whitney *U*-test. **(F)** Frequency of multilayered clones as a percentage of total clones. *n* = 4 midguts per genotype. *P* values by unpaired *t*-test.

For **(A-B, E-F)**, one of three independent experiments is shown with *n* numbers as specified for each experiment. For box-and-whisker plots, the boxes show median, 25th and 75th percentiles, and whiskers are minimum and maximum values. Representative images shown in each image panel.

Figure 4

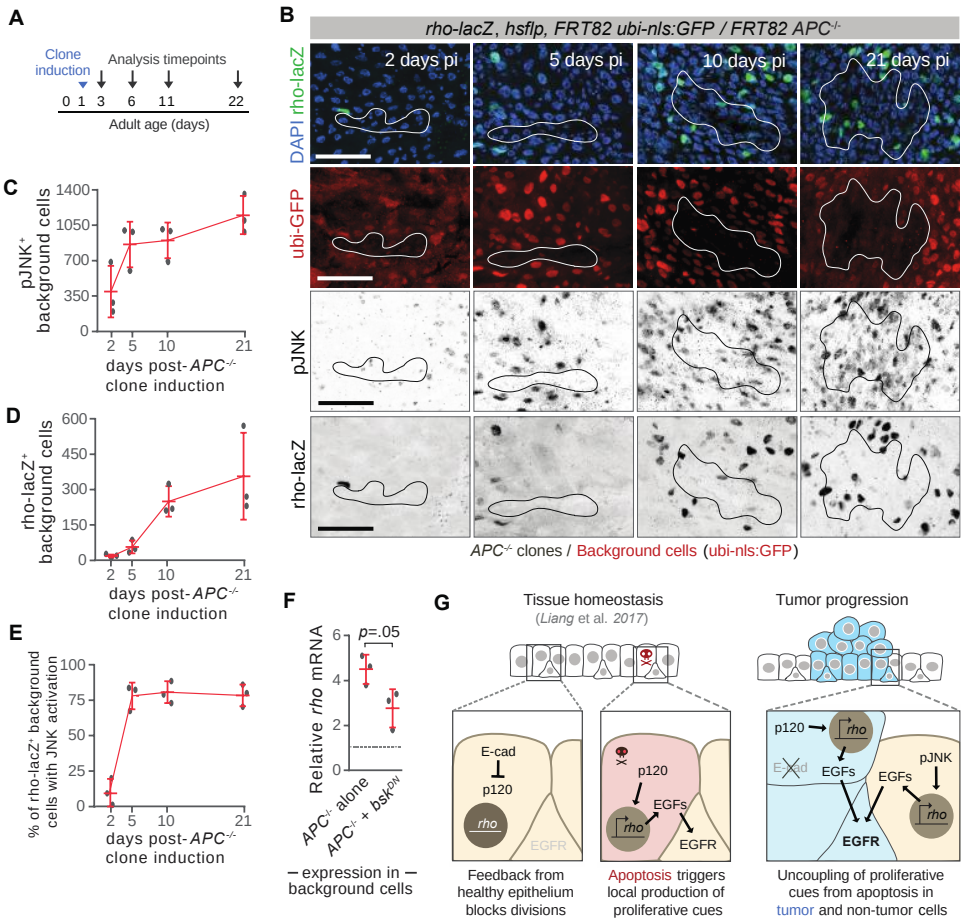

Figure 4. Nascent *APC*$^{-/-}$ clones induce *rhomboid* by eliciting JNK activation in background cells.

(A) Experimental timeline for B-E. *APC*$^{-/-}$ clones are induced in animals at 1 day post-eclosion and midguts are analyzed 2, 5, 10, and 21 days later.

(B-D) Background cells activate JNK before they hyper-induce *rhomboid*. **(B)** Images of midguts following immunostaining for activated, phosphorylated JNK (pJNK, inverted grayscale in third row) and *rhomboid-lacZ* (*rho-lacZ*; green in top row, inverted grayscale in bottom row) at the indicated times post-induction (pi) of *APC*$^{-/-}$ clones. Clone boundaries are outlined in white (top two rows) and black (bottom two rows).

Cells in clones lack GFP; background cells are marked by GFP (red pseudocolor). See Figure S2B for genetic strategy. Representative images are shown. Scale bars, 50 µm. **(C, D)** Numbers of background cells that are either pJNK$^+$ (C) or *rhomboid-lacZ*$^+$ (D) in midguts analyzed at the indicated times. Each data point represents one midgut. *n* = 3 midguts per timepoint; means ± S.D. One of three independent experiments is shown.

(E) Most background cells that express *rhomboid* also exhibit JNK activation. Graph shows the percentages of all *rhomboid*-lacZ$^+$ background cells that are also pJNK$^+$ in midguts analyzed at the indicated times. Each data point represents one midgut. *n* = 3 midguts per timepoint; means ± S.D. One of three independent experiments is shown.

(F) JNK activation in background cells promotes *rhomboid* hyper-induction. Graph shows levels of *rhomboid* mRNA, as measured by whole-midgut qPCR, in midguts of the indicated genotypes. Dotted gray line shows level of *rhomboid* mRNA in control midguts. Using the same experimental protocol as in Figure 3C, dominant negative JNK (*bsk*^{DN}) is expressed specifically in background cells and not in *APC*$^{-/-}$ cells. See Figures S2C, S3B for genetic strategy. Means ± S.D.; three biological replicates per condition. *P* values by unpaired *t*-test.

(G) Model. Tumor establishment requires that tumorigenic stem cells de-stabilize cell equilibrium by coercing cells to express *rhomboid* without apoptosis. During healthy turnover (left), stem cell division is coupled to enterocyte death because expression of *rhomboid*, and hence secretion of mitogenic EGFs, is linked to enterocyte apoptosis via apoptotic downregulation of E-cadherin and consequent release of p120-catenin [8]. For new tumors to become established (right), tumor-initiating stem cells must decouple division from death by instigating widespread expression of *rhomboid* in cells that are not apoptotic. *rhomboid* hyper-induction is initially tumor non-autonomous, via activation of JNK in background cells. It subsequently becomes tumor autonomous, via downregulation of E-cadherin and consequent activity of p120-catenin within tumor cells.

Supplementary Figures S1-S3

Supplementary Figure S1

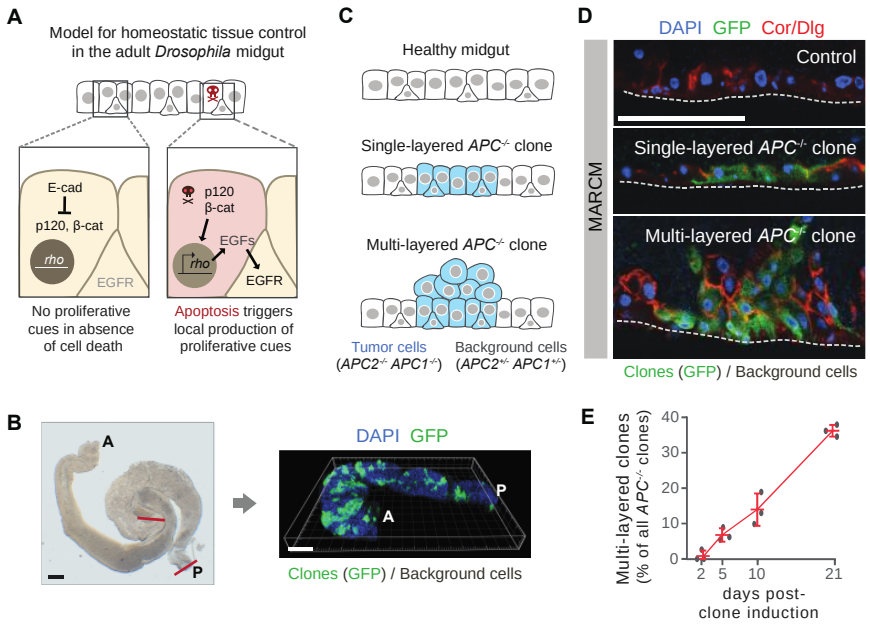

Supplementary Figure S1. Analysis of *APC*$^{-/-}$ clones in the adult *Drosophila* midgut.

(A) Cell equilibrium in the *Drosophila* adult midgut arises through coupling of stem cell divisions to enterocyte apoptosis. (Left) In the absence of enterocyte apoptosis, stem cells lack essential EGF mitogens and are therefore quiescent. Healthy enterocytes do not secrete EGFs because enterocyte E-cadherin prevents p120-catenin and β-catenin from activating transcription of the obligate EGF protease *rhomboid*. (Right) During physiological apoptosis, enterocytes downregulate E-cadherin. Loss of E-cadherin enables p120- and β-catenin to activate transcription of *rhomboid*. Rhomboid cleaves EGFs for secretion; the secreted EGFs activate nearby stem cells for replacement divisions. Cartoon adapted from [8].

(B) Midgut regions R4 and R5 were used for clonal analyses. (Left) Brightfield image of whole mount midgut. The R4-R5 regions [43] are demarcated by red lines. (Right) 3D reconstruction of R4 and R5 regions from a midgut that contains 21-day, GFP-labeled,

APC$^{-/-}$ clones (green). Clone size quantifications were performed by digitally isolating R4 and R5 in Fiji and visualizing the 3D reconstructed organ in Imaris. A=anterior, P=posterior. DAPI (blue) labels nuclei. Scale bars, 50 µm.

(C-D) Cellular organization of *APC*$^{-/-}$ clones. Cartoons **(C)** and images **(D)** show sagittal views of control tissue (top), a representative single-layered *APC*$^{-/-}$ clone (middle), and a representative multilayered *APC*$^{-/-}$ clone (bottom). The cellular organization of single-layered *APC*$^{-/-}$ clones resembles control tissue. The cellular organization of multilayered clones creates adenomatous masses that protrude into the midgut lumen. In D, immunostaining (red) for Coracle (Cor) and Discs large (Dlg) reveals cell outlines, and GFP (green) labels *APC*$^{-/-}$ clones, and DAPI (blue) labels all nuclei. Clones are 21 days post-induction.

(E) *APC*$^{-/-}$ clones progress from single-layered to multilayered over time. Graph shows the percent of all *APC*$^{-/-}$ clones that exhibit multilayering at 2, 5, 10, and 21 days after clone induction. Each data point represents one midgut. n = 3 midguts per timepoint; means ± S.D are shown. Scale bars, 50 µm.

Supplementary Figure S2

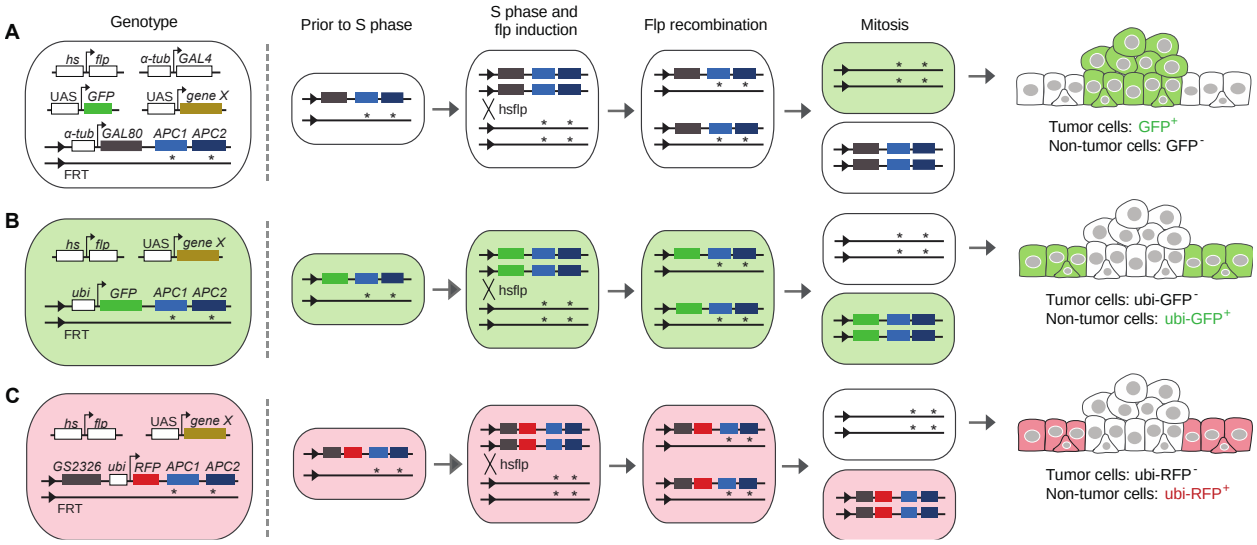

Supplementary Figure S2. Three genetic systems to generate and manipulate *APC*$^{-/-}$ clones.

In all three systems, all midgut cells are initially unlabeled and heterozygous for null alleles of *APC1* (*APC1*^{Q8}) and *APC2* (*APC2*^{G10}). Heat shock induces expression of *flp* recombinase, which catalyzes recombination in mitotic stem cells to generate a daughter cell that is homozygous for both *APC1*^{Q8} and *APC2*^{G10} (*APC*$^{-/-}$).

(A) Clone-autonomous labeling and manipulation. Schematic shows MARCM system to generate GFP-labeled *APC*$^{-/-}$ clones with concomitant genetic manipulation within clones. *Flp* recombination both generates an *APC*$^{-/-}$ daughter cell and eliminates *GAL80* specifically from that daughter. Loss of *GAL80* enables GAL4-driven expression of *UAS-GFP* and other *UAS*-transgenes (*UAS-gene X*) in the *APC*$^{-/-}$ cell and its progeny. Non-clone background cells remain unlabeled.

(B) Clone non-autonomous labeling. Schematic shows generation of unlabeled *APC*$^{-/-}$ clones within a background of GFP-labeled cells. All midgut cells initially express *ubi-GFP*. Heat-shock induction of *flp* recombinase produces an *APC*$^{-/-}$ daughter cell that lacks *ubi-GFP* and is thus unlabeled. Background cells continue to express *ubi-GFP*.

(C) Clone non-autonomous labeling and manipulation. Schematic shows the GeneSwitch 2326 system (also known as the “pLoser system” [24]), which generates unlabeled *APC*$^{-/-}$ clones with concomitant labeling and manipulation of background cells. Upon administration of RU486, *GeneSwitch-2326* (*GS2326*) [44] drives expression of *UAS*-transgenes (*UAS-gene X*) in midgut stem cells, enteroblasts, and enterocytes. Midgut cells initially express *ubi*-RFP and possess *GS2326*. Heat-shock induction of *flp* recombinase produces an *APC*$^{-/-}$ daughter cell that lacks *ubi-RFP* and *GS2326*. Background cells, which continue to express *ubi-RFP*, are capable of RU486-inducible expression of *UAS*-transgenes, whereas unlabeled *APC*$^{-/-}$ cells are not.

Supplementary Figure S3

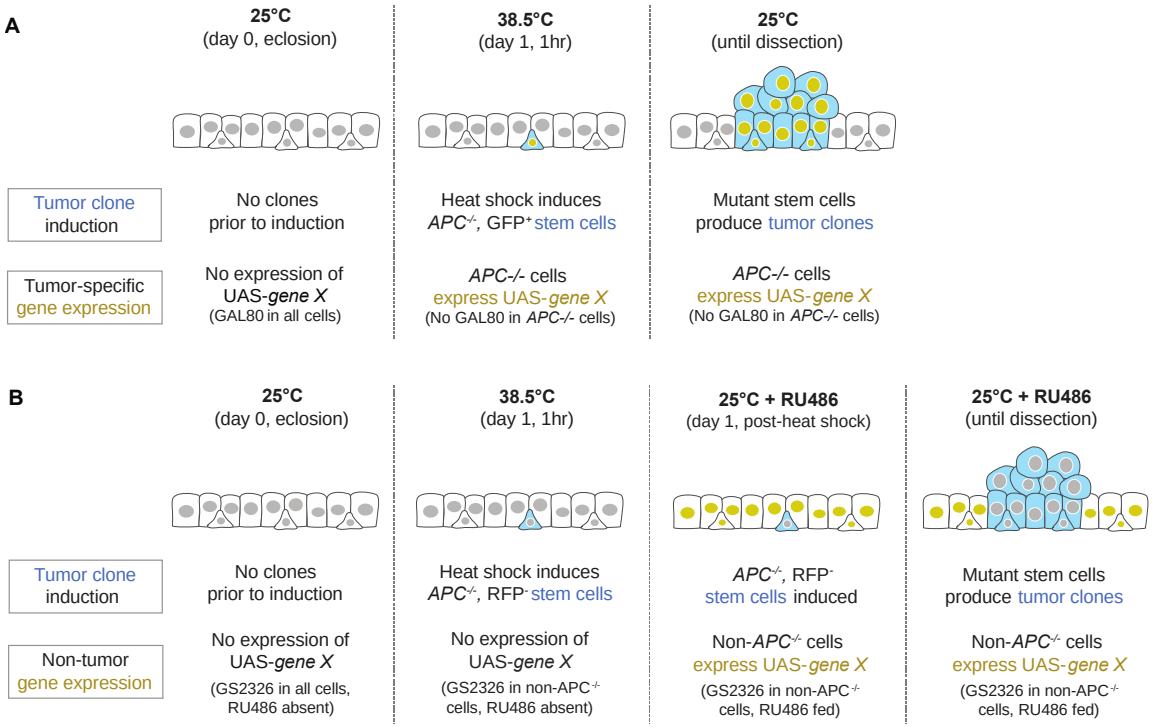

Supplementary Figure S3. Experimental protocols for induction of *APC*$^{-/-}$ clones and concomitant genetic manipulation.

(A) Clone-autonomous genetic manipulation using MARCM [18]. Animals eclose at 25ºC. Initially, all *UAS*-transgenes are silent due to ubiquitous expression of *tubGAL80*. At 1 day after eclosion, a 1-hour, 38.5ºC heat shock generates *APC*$^{-/-}$ mutant stem cells that have permanently lost *tubGAL80*. Loss of *tubGAL80* enables *tubGAL4*-driven expression of *UAS-GFP* and other *UAS*-transgenes (*UAS-geneX*) within *APC*$^{-/-}$ stem cells and any *APC*$^{-/-}$ stem cell progeny that are produced during the subsequent 25ºC chase. See also Figure S2A.

(B) Clone non-autonomous genetic manipulation using “pLoser” [24]. Animals eclose at 25º. Initially, *ubiRFP* is expressed in all cells; all *UAS*-transgenes are silent because *GeneSwitch-2326* (*GS2326*), which drives expression in enterocytes, enteroblasts, and stem cells, is inactive in the absence of RU486. At 1 day after eclosion, a 1-hour, 38.5ºC heat shock generates *APC*$^{-/-}$ mutant stem cells that have permanently lost both *ubi-RFP*

and *GS2326*. To activate expression of *UAS*-transgenes (*UAS-geneX*) in cells that retain *GS2326*, RU486 is administered immediately after heat shock and throughout the subsequent 25ºC chase. All cells that respond to RU486 (non-clone, background cells) also express *ubi-RFP.* By contrast, *APC*$^{-/-}$ stem cells and their progeny are unresponsive to RU486 and lack *ubi-RFP*. See also Figure S2C.

Supplementary Table 1 | Experimental genotypes by figure		
Figure	**Panels**	**Genotype**
Figure 1	Fig. 1B-C	*hsflp, UAS-GFP*; *tubGAL4 / E-cad^{mTomato}* ; *FRT82 tubGAL80 /* TM6B
		hsflp, UAS-GFP; *tubGAL4 / E-cad^{mTomato}*; *FRT82 tubGAL80 / FRT82, APC2^{G10}, APC1^{Q8}*
	Fig. 1F-H	*hsflp, UAS-GFP*; *tubGAL4*; *FRT82 tubGAL80 / FRT82*
		hsflp, UAS-GFP; *tubGAL4*; *FRT82 tubGAL80 / FRT82, APC2^{G10}, APC1^{Q8}*
		hsflp, UAS-GFP; *tubGAL4 / UAS-E-cad*; *FRT82 tubGAL80 / FRT82, APC2^{G10}, APC1^{Q8}*
		hsflp, UAS-GFP; *tubGAL4 / UAS-E-cad^{dCR4h}*; *FRT82 tubGAL80 / FRT82, APC2^{G10}, APC1^{Q8}*
		hsflp, UAS-GFP; *tubGAL4 / UAS-E-cad$^{\Delta JM}$*; *FRT82 tubGAL80 / FRT82, APC2^{G10}, APC1^{Q8}*
		hsflp, UAS-GFP; *tubGAL4 / UAS-p120* RNAi; *FRT82 tubGAL80 / FRT82, APC2^{G10}, APC1^{Q8}*
Figure 2	Fig. 2B-C	*hsflp; rho-lacZ (rho^{X81}), FRT82, ubi-GFP / FRT82*
	Fig. 2B-D	*hsflp; rho-lacZ (rho^{X81}), FRT82, ubi-GFP / FRT82, APC2^{G10}, APC1^{Q8}*
	Fig. 2E-F	*hsflp, UAS-GFP*; *tubGAL4*; *FRT82 tubGAL80 / FRT82*
		hsflp, UAS-GFP; *tubGAL4*; *FRT82 tubGAL80 / FRT82, APC2^{G10}, APC1^{Q8}*
	Fig. 2G-I	*hsflp, UAS-GFP*; *tubGAL4*; *FRT82 tubGAL80 / FRT82*
		hsflp, UAS-GFP; *tubGAL4*; *FRT82 tubGAL80 / FRT82, APC2^{G10}, APC1^{Q8}*
		hsflp, UAS-GFP; *tubGAL4 / UAS-egfr* RNAi; *FRT82 tubGAL80 / FRT82, APC2^{G10}, APC1^{Q8}*
		hsflp, UAS-GFP; *tubGAL4 / UAS-rho* RNAi; *FRT82 tubGAL80 / FRT82, APC2^{G10}, APC1^{Q8}*
Figure 3	Fig. 3A	*hsflp; rho-lacZ (rho^{X81}), FRT82, ubi-GFP / FRT82*
	Fig. 3A-B	*hsflp; rho-lacZ (rho^{X81}), FRT82, ubi-GFP / FRT82, APC2^{G10}, APC1^{Q8}*
	Fig. 3D-F	*hsflp*; *FRT82, GS2326, ubi-RFP / FRT82*
		hsflp; *FRT82, GS2326, ubi-RFP / FRT82, APC2^{G10}, APC1^{Q8}*
		hsflp; *UAS-egfr* RNAi; *FRT82, GS2326, ubi-RFP / FRT82, APC2^{G10}, APC1^{Q8}*
		hsflp; *UAS-E-cad*; *FRT82, GS2326, ubi-RFP / FRT82, APC2^{G10}, APC1^{Q8}*
		hsflp; *UAS-p120* RNAi; *FRT82, GS2326, ubi-RFP / FRT82, APC2^{G10}, APC1^{Q8}*
		hsflp; *UAS-rho* RNAi; *FRT82, GS2326, ubi-RFP / FRT82, APC2^{G10}, APC1^{Q8}*
Figure 4	Fig. 4B-E	*hsflp; rho-lacZ (rho^{X81}), FRT82, ubi-GFP / FRT82, APC2^{G10}, APC1^{Q8}*
	Fig. 4F	*hsflp*; *FRT82, GS2326, ubi-RFP / FRT82* (reference cDNA)
		hsflp; *FRT82, GSG2326, ubi-RFP / FRT82, APC2^{G10}, APC1^{Q8}*
		hsflp / UAS-bsk^{DN}; *FRT82, GSG2326, ubi-RFP / FRT82, APC2^{G10}, APC1^{Q8}*
Figure S1	Fig. S1B	*hsflp, UAS-GFP*; *tubGAL4*; *FRT82 tubGAL80 / FRT82, APC2^{G10}, APC1^{Q8}*
	Fig. S1D	*hsflp, UAS-GFP*; *tubGAL4 / E-cad^{mTomato}* ; *FRT82 tubGAL80 /* TM6B
		hsflp, UAS-GFP; *tubGAL4 / E-cad^{mTomato}*; *FRT82 tubGAL80 / FRT82, APC2^{G10}, APC1^{Q8}*
	Fig. S1E	*hsflp; rho-lacZ (rho^{X81}), FRT82, ubi-GFP / FRT82, APC2^{G10}, APC1^{Q8}*
Figure S2	Fig. S2A	*hsflp, UAS-GFP*; *tubGAL4*; *FRT82 tubGAL80 / FRT82, APC2^{G10}, APC1^{Q8}*
	Fig. S2B	*hsflp; FRT82, ubi-GFP / FRT82, APC2^{G10}, APC1^{Q8}*
	Fig. S2C	*hsflp*; *FRT82, GSG2326, ubi-RFP / FRT82, APC2^{G10}, APC1^{Q8}*
Figure S3	Fig. S3A	*hsflp, UAS-GFP*; *tubGAL4 / UAS-X*; *FRT82 tubGAL80 / FRT82, APC2^{G10}, APC1^{Q8}*
	Fig. S3B	*hsflp*; *UAS-X*; *FRT82, GSG2326, ubi-RFP / FRT82, APC2^{G10}, APC1^{Q8}*

'GS2326' denotes the GeneSwitch driver, *P[Switch]GSG2326* [24].

'*UAS-X*' generically denotes a UAS-driven transgene of interest (ex: *UAS-E-cad*)

Supplementary Table 2 | Clone numbers shown per figure panel				
Figure panel	**Condition**	**Total clones**	**No. of midguts**	**Clones per midgut**
Figure 1C	Early-stage *APC*$^{-/-}$	67	4*	14, 16, 17, 20
	Late-stage *APC*$^{-/-}$	38		8, 9, 10, 11
Figure 1G	Control	90	3	21, 33, 36
	APC$^{-/-}$ alone	79	3	22, 24, 33
	APC$^{-/-}$ + *E-cad*	79	3	24, 23, 32
	APC$^{-/-}$ + *E-cad*^{dCR4h}	97	3	24, 28, 45
	APC$^{-/-}$ + *E-cad*$^{\Delta JM}$	80	4	17, 20, 20, 23
	APC$^{-/-}$ + *p120* RNAi	116	3	29, 36, 51
Figure 2C	Control	81	3	26, 27, 28
	APC$^{-/-}$	47	4	11, 11, 12, 13
Figure 2F	Control	0	3	22, 32, 34
	APC$^{-/-}$	74	3	23, 25, 26
Figure 2H	Control	79	3	15, 25, 39
	APC$^{-/-}$ alone	74	3	23, 25, 26
	APC$^{-/-}$ + *egfr* RNAi	53	4	6, 11, 15, 21
	APC$^{-/-}$ + *rho* RNAi	83	3	24, 26, 33
Figure 3E	Control	75	3	24, 25, 26
	APC$^{-/-}$ alone	65	4	12, 14, 19, 20
	APC$^{-/-}$ + *egfr* RNAi	71	3	22, 23, 26
	APC$^{-/-}$ + *E-cad*	72	3	16, 28, 28
	APC$^{-/-}$ + *p120* RNAi	78	3	25, 26, 27
	APC$^{-/-}$ + *rho* RNAi	81	3	25, 26, 30

One of three repetitions is shown for each experiment; numbers of clones per experiment vary between repetitions.

*For Figure 1C, both early- and late-stage tumors were quantified from the same midguts (n = 4).

Materials and Methods

Drosophila husbandry

Adult female flies were used in all experiments. Crosses and adult flies were raised at 25°C. Unless specified otherwise, flies were heat-shocked 1 day after eclosion to induce clones and collected 21 days after induction for dissection/ immunostaining. See Supplementary Table 1 for full list of experimental genotypes.

Fly stocks

The following stocks were obtained from the Bloomington Stock Center: *y w shg*^{mTomato}, *UAS-shg, UAS-shg*$^{\Delta JM}$, *UAS-egfr* RNAi (TRiP.HMS05003), *UAS-rho* RNAi (TRiP.HMS02264), and *UAS-bsk*^{DN}. *UAS-p120* RNAi (KK113572) was obtained from the Vienna *Drosophila* Resource Center. The following stocks were generous gifts: *FRT82 APC2*^{G10} *APC1*^{Q8} (from M. Peifer), *hsflp; FRT82 ubi-GFP* and *hsflp*; *FRT82 GS2326 ubi-RFP* (from E. Piddini [24]), *UAS-shg*^{dCR4h} (from M. Fuller), and *rho*^{X81}(*rhomboid-lacZ,* from H. Jiang). Other stocks (from our previous studies [8, 45]): *w; FRT82* and *w UAS-CD8:GFP hsflp; tubGAL4; FRT82 tubGAL80*. Detailed information on *Drosophila* genes and stocks is available from FlyBase (http://flybase.org/).

Immunohistochemistry and microscopy

Samples were fixed, immunostained and mounted as previously described [8, 45]. Anti-GFP and anti-RFP antibodies were used to improve detection of *ubi-GFP* and *ubi-RFP* expression in tumor labeling systems (Figure S2). Anti-RFP was used to detect *shg*^{mTomato}. Primary antibodies: mouse anti-β-galactosidase (1:400, Promega Z3781), rabbit anti-cleaved caspase-3 (1:400, Cell Signaling, gift from D. Bilder), rabbit anti-dpErk (1:200, Cell Signaling 4370P), mouse anti-Coracle (1:400, DSHB C615.16), mouse anti-Discs large (1:400, DSHB 4F3), rabbit anti-pJNK pTPpY (1:500, Promega V7931), chicken anti-GFP (1:400, Invitrogen A10262) and rabbit anti-RFP (1:500, Invitrogen R10367). Secondary antibodies: Alexa Fluor 488-, 555- or 647-conjugated anti-rabbit, anti-mouse, or anti-chicken IgGs (1:800, LifeTechnologies A31570, A11001, A11039, A32728, A32732, and A21244). Nuclei were stained with DAPI

(LifeTechnologies, 1:1,000). Samples were mounted in ProLong (LifeTechnologies). Imaging of samples was performed on a Leica SP8 confocal microscope, with serial optical sections taken at 3.5-µm intervals through the entirety of whole-mounted, immunostained midguts.

Induction of stem cell clones

Tumor clones were generated using three separate labeling systems (Figure S2). For all three labeling systems, tumor clones were generated by collecting adult flies one day post-eclosion and performing two 30-min, 38.5°C heat shocks separated by a 8-min chill on ice. Flies were returned to 25°C until time of dissection. For experiments which manipulated gene expression in adjacent tissue after tumor induction (Figure S2C; also known as the "pLoser" system [24]), flies were fed RU486 upon returning to 25°C post-heat shock until time of dissection (see "GeneSwitch induction" below).

Clone visualization and cell counts

Tumors were visualized (1) as z-stacks using Fiji [46] and (2) in 3D using the Bitplane Imaris software. For each midgut, all clones within the R4 and R5 regions [43] were analyzed (see Figure S1B). Cells per tumor were measured as the number of $DAPI^+$ nuclei within the labeled clone boundary (as determined by the presence or absence of respective labeling proteins). All clone counts were performed manually. To categorize tumors as single-layered or multilayered, each tumor was viewed from the sagittal plane in Bitplane Imaris.

GeneSwitch induction

To induce expression of the GeneSwitch driver, *GS2326*, adult flies were fed RU486. RU486 (Sigma-Aldrich) was dissolved in dH_2O to reach a working concentration of 25 µg/mL. This solution was used to prepare yeast paste, which was fed to flies as a supplement to their standard cornmeal–molasses diet for the duration of induced gene expression. Drug-containing yeast paste was replenished every three days.

qRT-PCR

mRNA was extracted from whole midguts (four midguts per biological replicate) followed by cDNA synthesis with Invitrogen SuperStrand III First Script Super Mix (Invitrogen). Real-time PCR was performed using the relative standard curve method with SYBR GreenER Supermix (Invitrogen) on a StepOnePlus ABI machine. Each biological replicate was assessed in three technical replicate experiments. Expression levels were normalized to non-tumorous midguts expressing control clones; *rp49* transcripts were used as a reference. Primers were from [8, 47]. Primer sequences from 5' to 3' – *rp49* Fwd: CGGATCGATATGCTAAGCTGT, *rp49* Rev: CGACGCACTCTGTTGTCG, *rhomboid* Fwd: GAGCACATCTACATGCAACGC, and *rhomboid* Rev: GGAGATCACTAGGATGAACCAGG.

Statistical analysis

All statistical analyses were performed using Graphpad Prism 7. For comparisons of clone size distributions, unpaired two-tailed Mann–Whitney *U*-tests were used to assess statistical significance. To compare the frequencies of mutilayered clones, cell numbers or percentages, and mRNA levels, unpaired two-tailed *t*-tests were used to assess statistical significance.

Study design

Sample sizes were chosen based on our previous studies [8, 45], which also characterized changes in clone sizes and midgut cell numbers; see also Supplementary Table 2. No exclusion criteria were applied. No sample randomization or blinding was performed.

References

1. Pellettieri, J., and Sanchez Alvarado, A. (2007). Cell turnover and adult tissue homeostasis: from humans to planarians. Annu Rev Genet *41*, 83-105.
2. O'Brien, L.E., and Bilder, D. (2013). Beyond the niche: tissue-level coordination of stem cell dynamics. Annu Rev Cell Dev Biol *29*, 107-136.
3. Brown, S., Pineda, C.M., Xin, T., Boucher, J., Suozzi, K.C., Park, S., Matte-Martone, C., Gonzalez, D.G., Rytlewski, J., Beronja, S., et al. (2017). Correction of aberrant growth preserves tissue homeostasis. Nature *548*, 334-337.
4. Patel, P.H., Dutta, D., and Edgar, B.A. (2015). Niche appropriation by Drosophila intestinal stem cell tumours. Nat Cell Biol *17*, 1182-1192.
5. Egeblad, M., Nakasone, E.S., and Werb, Z. (2010). Tumors as organs: complex tissues that interface with the entire organism. Dev Cell *18*, 884-901.
6. Brock, A., Krause, S., and Ingber, D.E. (2015). Control of cancer formation by intrinsic genetic noise and microenvironmental cues. Nat Rev Cancer *15*, 499-509.
7. Quail, D.F., and Joyce, J.A. (2013). Microenvironmental regulation of tumor progression and metastasis. Nat Med *19*, 1423-1437.
8. Liang, J., Balachandra, S., Ngo, S., and O'Brien, L.E. (2017). Feedback regulation of steady-state epithelial turnover and organ size. Nature *548*, 588-591.
9. Tian, A., Benchabane, H., and Ahmed, Y. (2018). Wingless/Wnt Signaling in Intestinal Development, Homeostasis, Regeneration and Tumorigenesis: A Drosophila Perspective. J Dev Biol *6*.
10. Rodriguez, F.J., Lewis-Tuffin, L.J., and Anastasiadis, P.Z. (2012). E-cadherin's dark side: possible role in tumor progression. Biochim Biophys Acta *1826*, 23-31.
11. Brooks, S.A., Lomax-Browne, H.J., Carter, T.M., Kinch, C.E., and Hall, D.M. (2010). Molecular interactions in cancer cell metastasis. Acta Histochem *112*, 3-25.
12. Yu, Y., and Elble, R.C. (2016). Homeostatic Signaling by Cell-Cell Junctions and Its Dysregulation during Cancer Progression. J Clin Med *5*.
13. Jeanes, A., Gottardi, C.J., and Yap, A.S. (2008). Cadherins and cancer: how does cadherin dysfunction promote tumor progression? Oncogene *27*, 6920-6929.
14. Roskoski, R. (2014). The ErbB/HER family of protein-tyrosine kinases and cancer. Pharmacol Res *79*, 34-74.
15. Yewale, C., Baradia, D., Vhora, I., Patil, S., and Misra, A. (2013). Epidermal growth factor receptor targeting in cancer: a review of trends and strategies. Biomaterials *34*, 8690-8707.
16. Cheng, T.L., Lai, C.H., Jiang, S.J., Hung, J.H., Liu, S.K., Chang, B.I., Shi, G.Y., and Wu, H.L. (2014). RHBDL2 is a critical membrane protease for anoikis resistance in human malignant epithelial cells. Scientific World Journal *2014*, 902987.
17. Song, W., Liu, W., Zhao, H., Li, S., Guan, X., Ying, J., Zhang, Y., Miao, F., Zhang, M., Ren, X., et al. (2015). Rhomboid domain containing 1 promotes

colorectal cancer growth through activation of the EGFR signalling pathway. Nature Communications *6*, 8022.
18. Lee, T., and Luo, L. (1999). Mosaic analysis with a repressible cell marker for studies of gene function in neuronal morphogenesis. Neuron *22*, 451-461.
19. Ahmed, Y., Hayashi, S., Levine, A., and Wieschaus, E. (1998). Regulation of armadillo by a Drosophila APC inhibits neuronal apoptosis during retinal development. Cell *93*, 1171-1182.
20. McCartney, B.M., Price, M.H., Webb, R.L., Hayden, M.A., Holot, L.M., Zhou, M., Bejsovec, A., and Peifer, M. (2006). Testing hypotheses for the functions of APC family proteins using null and truncation alleles in Drosophila. Development *133*, 2407-2418.
21. Lee, W.C., Beebe, K., Sudmeier, L., and Micchelli, C.A. (2009). Adenomatous polyposis coli regulates Drosophila intestinal stem cell proliferation. Development *136*, 2255-2264.
22. Wang, C., Zhao, R., Huang, P., Yang, F., Quan, Z., Xu, N., and Xi, R. (2013). APC loss-induced intestinal tumorigenesis in Drosophila: Roles of Ras in Wnt signaling activation and tumor progression. Dev Biol *378*, 122-140.
23. Cordero, J.B., Stefanatos, R.K., Myant, K., Vidal, M., and Sansom, O.J. (2012). Non-autonomous crosstalk between the Jak/Stat and Egfr pathways mediates Apc1-driven intestinal stem cell hyperplasia in the Drosophila adult midgut. Development *139*, 4524-4535.
24. Suijkerbuijk, S.J., Kolahgar, G., Kucinski, I., and Piddini, E. (2016). Cell Competition Drives the Growth of Intestinal Adenomas in Drosophila. Curr Biol *26*, 428-438.
25. Tian, A., Benchabane, H., Wang, Z., Zimmerman, C., Xin, N., Perochon, J., Kalna, G., Sansom, O.J., Cheng, C., Cordero, J.B., et al. (2017). Intestinal stem cell overproliferation resulting from inactivation of the APC tumor suppressor requires the transcription cofactors Earthbound and Erect wing. PLoS Genet *13*, e1006870.
26. Fearon, E.R. (2011). Molecular genetics of colorectal cancer. Annu Rev Pathol *6*, 479-507.
27. Dorudi, S., Sheffield, J.P., Poulsom, R., Northover, J.M., and Hart, I.R. (1993). E-cadherin expression in colorectal cancer. An immunocytochemical and in situ hybridization study. Am J Pathol *142*, 981-986.
28. Hao, X., Palazzo, J.P., Ilyas, M., Tomlinson, I., and Talbot, I.C. (1997). Reduced expression of molecules of the cadherin/catenin complex in the transition from colorectal adenoma to carcinoma. Anticancer research *17*, 2241-2247.
29. Huang, J., Zhou, W., Dong, W., Watson, A.M., and Hong, Y. (2009). Directed, efficient, and versatile modifications of the Drosophila genome by genomic engineering. Proc Natl Acad Sci U S A *106*, 8284-8289.
30. Oda, H., and Tsukita, S. (1999). Nonchordate classic cadherins have a structurally and functionally unique domain that is absent from chordate classic cadherins. Dev Biol *216*, 406-422.
31. McCrea, P.D., and Gottardi, C.J. (2016). Beyond β-catenin: prospects for a larger catenin network in the nucleus. Nat Rev Mol Cell Biol *17*, 55-64.

32. Pacquelet, A., and Rørth, P. (2005). Regulatory mechanisms required for DE-cadherin function in cell migration and other types of adhesion. J Cell Biol *170*, 803-812.
33. Huels, D.J., Ridgway, R.A., Radulescu, S., Leushacke, M., Campbell, A.D., Biswas, S., Leedham, S., Serra, S., Chetty, R., Moreaux, G., et al. (2015). E-cadherin can limit the transforming properties of activating β-catenin mutations. EMBO J *34*, 2321-2333.
34. Phelps, R.A., Chidester, S., Dehghanizadeh, S., Phelps, J., Sandoval, I.T., Rai, K., Broadbent, T., Sarkar, S., Burt, R.W., and Jones, D.A. (2009). A two-step model for colon adenoma initiation and progression caused by APC loss. Cell *137*, 623-634.
35. Cordero, J.B., Ridgway, R.A., Valeri, N., Nixon, C., Frame, M.C., Muller, W.J., Vidal, M., and Sansom, O.J. (2014). c-Src drives intestinal regeneration and transformation. EMBO J *33*, 1474-1491.
36. Jiang, H., Patel, P.H., Kohlmaier, A., Grenley, M.O., McEwen, D.G., and Edgar, B.A. (2009). Cytokine/Jak/Stat signaling mediates regeneration and homeostasis in the Drosophila midgut. Cell *137*, 1343-1355.
37. Jiang, H., Grenley, M.O., Bravo, M.J., Blumhagen, R.Z., and Edgar, B.A. (2011). EGFR/Ras/MAPK signaling mediates adult midgut epithelial homeostasis and regeneration in Drosophila. Cell Stem Cell *8*, 84-95.
38. Zhai, Z., Kondo, S., Ha, N., Boquete, J.P., Brunner, M., Ueda, R., and Lemaitre, B. (2015). Accumulation of differentiating intestinal stem cell progenies drives tumorigenesis. Nat Commun *6*, 10219.
39. Ma, X., Shao, Y., Zheng, H., Li, M., Li, W., and Xue, L. (2013). Src42A modulates tumor invasion and cell death via Ben/dUev1a-mediated JNK activation in Drosophila. Cell Death Dis *4*, e864.
40. Lacunza, E., Canzoneri, R., Rabassa, M.E., Zwenger, A., Segal-Eiras, A., Croce, M.V., and Abba, M.C. (2012). RHBDD2: a 5-fluorouracil responsive gene overexpressed in the advanced stages of colorectal cancer. Tumour Biol *33*, 2393-2399.
41. Tsanou, E., Peschos, D., Batistatou, A., Charalabopoulos, A., and Charalabopoulos, K. (2008). The E-cadherin adhesion molecule and colorectal cancer. A global literature approach. Anticancer Res *28*, 3815-3826.
42. Zhang, M., Miao, F., Huang, R., Liu, W., Zhao, Y., Jiao, T., Lu, Y., Wu, F., Wang, X., Wang, H., et al. (2018). RHBDD1 promotes colorectal cancer metastasis through the Wnt signaling pathway and its downstream target ZEB1. J Exp Clin Cancer Res *37*, 22.
43. Buchon, N., Osman, D., David, F.P., Fang, H.Y., Boquete, J.P., Deplancke, B., and Lemaitre, B. (2013). Morphological and molecular characterization of adult midgut compartmentalization in Drosophila. Cell Rep *3*, 1725-1738.
44. Roman, G., Endo, K., Zong, L., and Davis, R.L. (2001). P[Switch], a system for spatial and temporal control of gene expression in Drosophila melanogaster. Proc Natl Acad Sci U S A *98*, 12602-12607.
45. O'Brien, L.E., Soliman, S.S., Li, X., and Bilder, D. (2011). Altered modes of stem cell division drive adaptive intestinal growth. Cell *147*, 603-614.

46. Schindelin, J., Arganda-Carreras, I., Frise, E., Kaynig, V., Longair, M., Pietzsch, T., Preibisch, S., Rueden, C., Saalfeld, S., Schmid, B., et al. (2012). Fiji: an open-source platform for biological-image analysis. Nat Methods *9*, 676-682.
47. Amcheslavsky, A., Song, W., Li, Q., Nie, Y., Bragatto, I., Ferrandon, D., Perrimon, N., and Ip, Y.T. (2014). Enteroendocrine cells support intestinal stem-cell-mediated homeostasis in Drosophila. Cell Rep *9*, 32-39.